

A high-performance lung-inspired ceramic 3D-printed heat exchanger for high-temperature energy-efficient systems

Behzad Ahmadi^a, Joseph Cesarano^b, Kashif Nawaz^c, Nikolas Ninoss^d, Sajjad Bigham^{c,*}

^a Department of Mechanical Engineering-Engineering Mechanics, Michigan Technological University, 1400 Townsend Drive, Houghton, MI, 49931-1295, USA

^b Robocasting Enterprises, Albuquerque, NM, 87109, USA

^c Building Technologies Research and Integration Center, Oak Ridge National Laboratory, One Bethel Valley Road, P.O. Box 2008, MS-6070, Oak Ridge, TN, 37831-6070, USA

^d Calix Ceramic Solutions, Buffalo, NY 14228, USA

Abstract

The heat-to-electricity conversion efficiency of next-generation supercritical carbon dioxide and concentrated solar power plants is significantly augmented by operating at temperatures exceeding 1000°C if durable compact high-temperature heat exchangers (HXs) are developed. Whereas metal 3D-printed HXs fail to operate under extreme temperature conditions, ceramic 3D-printed HXs are deemed promising candidates for high-temperature, highly oxidizing environments. Ceramic stereolithography 3D-printed HXs, however, exhibit a high gas permeability issue through hot and cold separating walls due to an excessive non-volatile photopolymer content utilized. Here, a novel leak-free lung-inspired ceramic 3D-printed HX employing a highly complex heat transfer topology is introduced for high-temperature energy-efficient systems. The high permeability issue of ceramic 3D-printed HXs is fully eliminated through a uniform zirconia-based coating. It was found that the effective thermal conductivity of the sintered ceramic 3D-printed HX is affected by the coated layer. The high-temperature thermo-hydraulic characteristics of the lung-inspired ceramic 3D-printed HX are comprehensively examined and compared against a plate-and-frame robocasted 3D-printed HX module. Experimental results indicated that the lung-inspired 3D-printed HX significantly outperforms its plate-and-frame counterpart. The volume-based power density of the lung-inspired HX is 8.2 MW/m³ at a hot-side inlet air temperature of 700°C, a 71% improvement compared with that of the plate-and-frame HX. More importantly, the higher thermal performance of the lung-inspired 3D-printed HX is realized at a lower normalized pressure drop penalty of 510 Pa/W, a 22% reduction compared with its plate-and-frame counterpart. The insights gained from this study could offer new pathways to design innovative high-performance leak-free ceramic 3D-printed HXs for high-temperature energy-efficient systems and/or corrosive environments.

Keywords: Ceramic 3D-printed heat exchanger; Lung-inspired heat exchanger topology; High-temperature heat exchanger; Stereolithography 3D-printing; Robocasted 3D-printing.

1. Introduction

A significant portion of primary energy utilized in several key industrial applications including conventional and advanced power generation cycles, aviation, and metal/glass production is currently wasted at high temperatures. More importantly, next-generation supercritical carbon dioxide and concentrated solar power plants [1], future on-demand

* Corresponding author. Tel.: +1 906 487 2747.

Email address: sbigham@mtu.edu (S. Bigham)

mobility and air-transport-class aircraft, and very-high-temperature reactor (VHTR) concepts are all expected to operate at temperatures exceeding 1000°C under extreme environments. A substantial improvement in thermal conversion efficiency accompanied by a simultaneous reduction in fuel consumption, system footprint, and carbon dioxide emissions can be realized if the high-temperature thermal energy can be harvested in the case of industrial waste heat recovery or exchanged in the case of future power and mobility systems. Current heat exchanger technologies, however, fail under severe operating conditions imposed by high temperatures present in several aforementioned applications.

State-of-the-art materials for high-temperature heat exchanger applications are metals and superalloys including high-grade steels and nickel-based alloys. For instance, compact metallic printed circuit heat exchangers (PCHXs) have been proposed for supercritical carbon dioxide power plants [2,3]. Heat exchangers made of metals and superalloy materials, however, experience an intense degradation in critical material properties at elevated temperatures and particularly lose their strength at temperatures exceeding 800°C [4]. Ceramic heat exchangers (CHXs), on the other hand, offer favorable high-temperature thermo-mechanical properties including superior mechanical strength and excellent corrosion, oxidation, creep, wear, and abrasion resistance, thereby making them a promising alternative solution to metallic heat exchangers. In addition, the thermal conductivity of several ceramic materials including alumina and silicon carbide is as high as that of stainless steel.

Banerjee et al. [5] examined the thermal performance of a counterflow tube-in-tube alumina reticulated porous ceramic (RPC) HX to recover heat from gases flowing through a solar thermochemical reactor. The HX was comprised of two concentric alumina tubes, each filled with alumina reticulated porous ceramic with a nominal porosity of 80% and pore density of 5 pores per inch. At a hot inlet temperature of 1240 K and a laminar flow regime, experimental results predicted a maximum overall heat transfer coefficient of 41 W/m²K⁻¹ and effectiveness up to 73%. Kee et al. [6] designed and tested a compact microchannel alumina HX using a fabrication process called pressure laminated integrated structures (PLIS). An HX effectiveness of 70% was reported at hot and cold inlet temperatures of 750 and 25°C, respectively. Fend et al. [7] examined the thermal performance of a ceramic HX utilizing honeycomb structures made of extruded silicon carbide. An HX effectiveness of 65% at a hot inlet temperature of 950°C was obtained. Haunstetter et al. [8] evaluated the thermal performance of a silicon carbide plate-fin HX for power plant applications and high-temperature processes. The HX was fabricated using a six-step manufacturing process of (i) production of green compact plates, (ii) sintering of the plates, (iii) combining every two plates, (iv) application of an environmental barrier coating, (v) join sintering, and (vi) final assembly. At a temperature of 800°C and a pressure of 5 bar, experimental results showed a high effectiveness range of 65-97%. However, the above ceramic HXs are limited to conventional manufacturing techniques with constraints on design freedom for enhanced heat transfer topologies and ease of the manufacturing process.

Eliminating traditional fabrication limitations, additive manufacturing (AM) enables fabrication of complex topologies with augmented heat transfer characteristics for next-generation high-temperature HXs. AM also allows rapid and cost-effective prototyping, reduces energy use and material wastes, and shortens time to market for small to medium-sized production. This is particularly advantageous to the manufacturing of high-temperature HXs

in which fabrication typically involves custom-made and/or some highly difficult-to-machine ceramic materials. Limited studies have focused on thermal performance evaluations of ceramic 3D-printed HXs. Schwarzer et al. [9] and Scheithauer et al. [10] explored the feasibility of a lithography ceramic manufacturing (LCM) technique for HX applications. They identified suspension development and cleaning from ceramic AM components as two main steps of the LCM process chain. Shulman et al. [11] fabricated a zirconia toughened mullite (ZTM) HX using the laminated object manufacturing (LOM) technique. It was detected that the leakage from the cold to the hot side was a major issue leading to flow mixing and an inflated heat transfer, thereby making the experimentally measured thermal performance values deviate from their predicted values. Employing an extrusion freeform fabrication (EFF) technique, Bower et al. [12] fabricated a water-cooled milli-channel silicon carbide heat sink for electronic cooling applications. Thermo-hydraulic performances of several silicon carbide heat sinks with different topologies were compared against a copper heat sink. It was found that, despite its lower thermal conductivity, the silicon carbide heat sink compares favorably with the copper heat sink at similar overall flow rates. However, the above ceramic 3D-printed HXs employ simple heat exchanger designs, and thus do not fully exploit design freedoms offered by ceramic 3D printing. Additionally, their thermal performance, durability, and reliability have not yet been examined for high-temperature heat recovery applications. Furthermore, the gas leakage between the hot and cold flow channels remains an issue for advanced ceramic 3D-printed HXs.

To address the aforementioned scientific and technological gaps, this study introduces and examines an innovative leak-free lung-inspired ceramic 3D-printed heat exchanger topology for high-temperature heat recovery applications. The new heat transfer geometry is tailored to create a balance between enhanced thermal exchange rate and induced pressure drop penalty. The high-temperature thermal performance of the lung-inspired ceramic 3D-printed HX is compared against that of a plate-and-frame 3D-printed HX module. In the following, first, the proposed lung-inspired HX and its unique features are introduced. Next, the two-examined ceramic 3D-printing techniques are reviewed. Then, the experimental test facility and numerical procedure are discussed. Finally, the high-temperature thermal performance of the lung-inspired ceramic HX topology at various thermo-hydraulic conditions is comprehensively discussed.

2. Lung-inspired ceramic HX topology

The conceptual design of the proposed ceramic HX topology is inspired by the bronchi architecture of human lungs demonstrating an improved volumetric flow distribution. Figs. 1a-c show an actual image and schematics of the lung-inspired ceramic HX design. At the heart of the HX design, there is a representative cell (cf. Fig. 1b) with a trifurcating network of channels exhibiting three converging inlet and diverging outlet pathways each of which at a different 3D spatial orientation. This allows the evolution of two intertwined bicontinuous flow networks for an efficient heat transfer process between hot and cold sides at a reduced pressure drop penalty. The first network (i.e., the red color in Fig. 1c) volumetrically splits an incoming hot air stream into multiple connected channels that are spread out within the second cold network. The second network (i.e., the blue color in Fig. 1c) distributes the cold air stream within and through the first hot network, thereby allowing an intimate contact area with a

reduced thermal resistance between hot and cold air streams for an augmented heat transport process. Fig. 1a shows an image of the lung-inspired silica HX that is 3D-printed using the stereolithography (SLA) technique. The overall dimensions and mass of the lung-inspired silica HX are $33.2 \times 35.2 \times 33.3 \text{ mm}^3$ and 84.35 g, respectively. The thickness of curved separating walls is 2 mm. It is worth noting that the durability of the SLA 3D-printed silica HX was evaluated using a torch flame at a temperature exceeding 1100°C as illustrated in Fig. 1d.

A plate-and-frame alumina HX employing milli-channels (cf. Fig. 1e) was also 3D-printed using the robocasting method as a reference HX design. The plate-and-frame ceramic HX was designed and tested in a counter-flow arrangement as shown in Fig. 1e. The HX includes twelve hot and twelve cold flow channels (cf. Fig. 1f). Each channel has a cross-sectional area of $1.5 \times 1.6 \text{ mm}^2$ (cf. Fig. 1g) with a length of 40 mm. The thickness of the separating walls between the hot and cold flow channels is 2 mm. The weight of the plate-and-frame milli-channel HX is 119.5 g. Additionally, a cross-sectional computerized tomography (CT) scan of the sintered plate-and-frame HX design is shown in Fig. 1g exhibiting a high-quality leak-free 3D-printed HX module with no large and/or connected voids, thereby eliminating any post-treatment step.

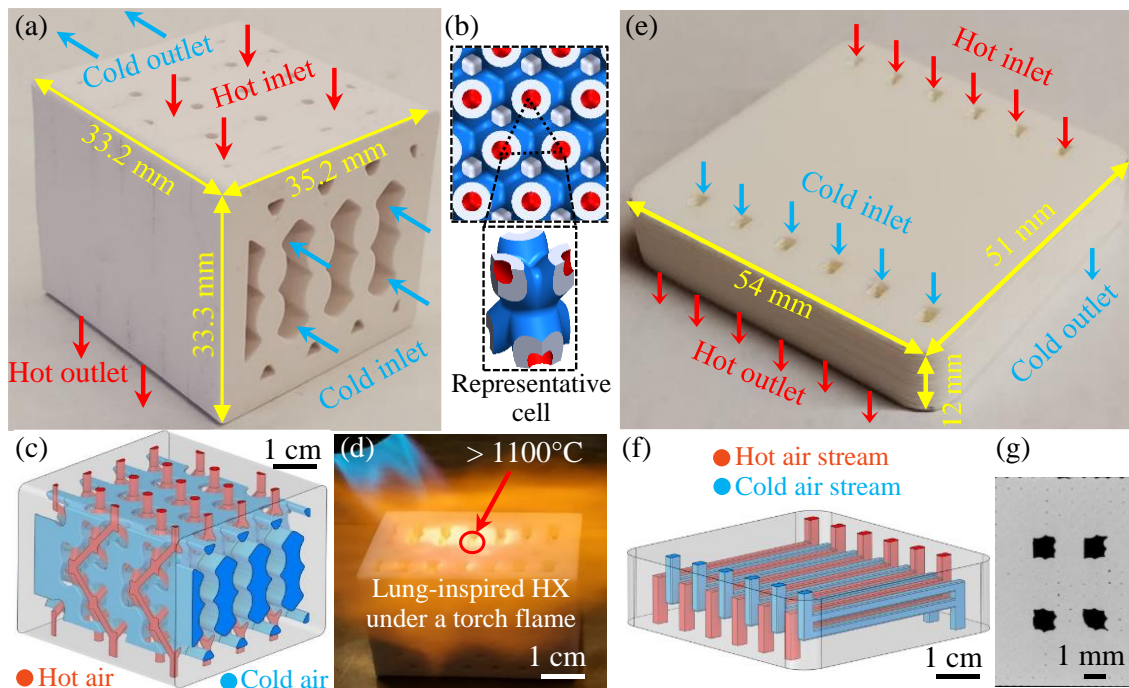


Fig. 1. (a) An image of the lung-inspired silica 3D-printed HX module, (b and c) 2D and 3D views of the two intertwined bicontinuous cold and hot flow networks, (d) the lung-inspired silica 3D-printed HX module under a torch flame, (e and f) an image and a 3D schematic of the plate-and-frame alumina HX module, (f) a 3D schematic of the plate-and-frame HX, and (g) a cross-sectional CT scan of the sintered plate-and-frame alumina HX module.

3. Ceramic 3D-printing

In this study, SLA and robocasting 3D-printing techniques were employed to fabricate the lung-inspired silica and plate-and-frame alumina HX modules, respectively. The SLA approach enables 3D-printing of highly complex topologies but shows a severe leakage issue through walls separating the hot and cold fluids. In contrast, the robocasting technique relies on the extrusion of a high-quality slurry with minimum fugitive ‘plasticizing’ materials, thereby resulting in high-quality leak-free HX modules. However, the robocasting technique

does not allow 3D-printing of highly complex HX structures. In the following, the two 3D-printing approaches are discussed.

3.1. The SLA 3D-printing method

The SLA method is a laser-based 3D-printing system employing a liquid photopolymer resin sensitive to ultraviolet light. A schematic of the SLA method is shown in Fig. 2a. The resin exposed to the laser beam is selectively hardened to create a desired patterned layer. The hardened layer is then moved up in a small increment creating a narrow space that allows the uncured resin to enter and be selectively cured. The process is repeated layer-by-layer until a model is created. This enables ceramic 3D-printing of highly complex topologies. The SLA technique also requires support for overhangs and cavities. In this work, the lung-inspired silica HX module is 3D-printed using Formlabs' Form 2 3D-printer. A layer thickness of 100 microns was chosen for 3D-printing. Upon 3D-printing, the green 3D-printed part was sintered at 1270°C to vaporize the photo-cured polymer resin and densify the ceramic part. Preliminary leakage tests showed that the sintered silica HX module was highly porous. A zirconia-based coating was then developed and applied to the ceramic 3D-printed HX module. The coated HX module was again sintered at 1270°C to harden the coating layer. The result was a high-quality leak-proof ceramic 3D-printed HX module. Dimensions and weight of the lung-inspired silica HX at different stages of the fabrication process are listed in Table 1.

Table 1. Dimensions and weight of the lung-inspired silica HX at different fabrication stages.

Stage	Length (mm)	Width (mm)	Height (mm)	Weight (g)
Green part	40.1	39.1	37.2	118.5
Sintered part	34.6	36.5	34.4	80.5
Final coated part	33.2	35.2	33.3	84.35

3.2. The robocasting 3D-printing method

Robocasting, on the other hand, is a direct ink writing (DIW) technique in which a 3D topology is printed layer-by-layer through extrusion and deposition of a ceramic slurry [13]. A schematic of the robocasting method is shown in Fig. 2b. In contrast to other extrusion-based 3D-printing techniques employing more than 50% non-volatile organic additives which cause considerable voids upon sintering, the robocasting technique limits organic additives to a maximum of less than 2% by volume fraction

[14]. This small fraction of organic additives is then removed during sintering without causing a major defect in the final sintered part. Moreover, the robocasting technique is a rapid moldless approach in which a ceramic module is 3D-printed, dried, and sintered in less than 24 hours. The robocasting technique is divided into 3 main sub-steps of slurry preparation, slurry delivery, and sintering of a green body as discussed in the following.

Slurry preparation: The slurry for the robocasting method usually includes a volatile solvent (typically water), a ceramic powder (e.g., Al_2O_3), and a small amount of a non-volatile organic

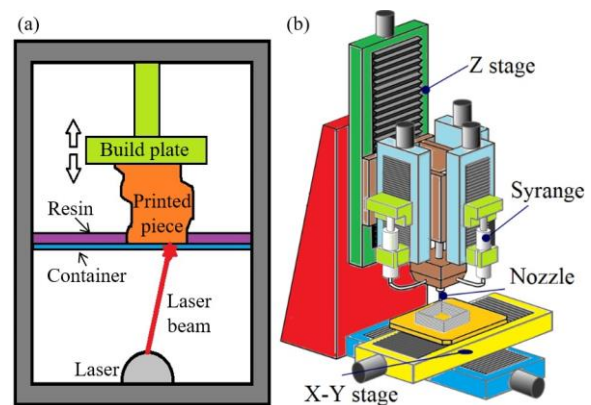


Fig. 2. Schematics of (a) the SLA, and (b) robocasting 3D-printing techniques.

binder. The rheological behavior of a ceramic slurry is an important factor affecting the quality of the final sintered product. Fig. 3 shows the effect of solid volume fraction on the viscosity of a ceramic slurry. The viscosity of the dispersed slurry is low at a small solid volume fraction (i.e., a Newtonian regime). The rheological behavior of the ceramic slurry changes from a Newtonian to a pseudoplastic regime as the solid content increases. At around 60 vol% solid content, particle collisions become dominant. With a further increase in the solid volume fraction, the mobility of ceramic particles is restricted, and the ceramic slurry moves to a dilatant regime [16]. If the slurry viscosity is low, beads are loose and cannot properly settle on a printed layer. If the slurry viscosity is high, on the other hand, beads have a circular cross-section and thus a minimum contact area with a previously dispersed layer leading to a lower structural strength. Achieving a rectangular cross-sectional area with straight walls and a flat top section is an optimal condition. To realize this state, the slurry rheology should be in the pseudoplastic regime, but close to the dilatant regime. Under this condition, with a minimum drying during the 3D-printing process, the volatile solvent (i.e., water) evaporates and the volume percentage of the solid ceramic power increases to the dilatant regime. Thereby, the pseudoplastic behavior of the ceramic slurry causes a smooth slurry flow during dispersion, but solidification during deposition so the slurry bead can retain its shape [15]. It should be noted that the drying rate is also important. If the drying rate is too slow, the transformation from the pseudoplastic to the dilatant regime is delayed and thus the weight of several printed layers can exceed the yield stress of the lower layers. In contrast, if the drying rate is too high, it might cause cracking and delamination in the final product. In this study, the alumina feedstock for 3D-printing of the plate-and-frame HX module contains approximately 38 vol% volatile solvent, 60 vol% alumina powder, and less than 2 vol% organic additives.

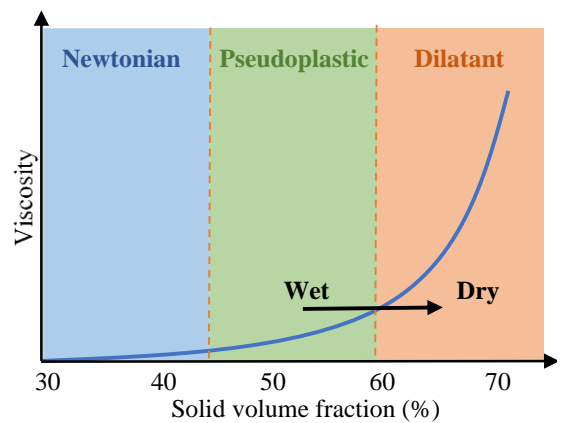


Fig. 3. Effect of solid volume fraction on slurry viscosity.

Slurry delivery: Several 3D-printing parameters including tool path, extrusion flow rate, nozzle architecture, drying rate of a deposited layer, and platform temperature should be carefully controlled to avoid possible defects either during 3D-printing or sintering step. In contrast to a droplet-based DIW, the robocasting technique is a filament-based DIW relying on a continuous ceramic filament deposited on a warm platform or a previously printed layer [14]. Any discontinuity in the ceramic slurry filament during deposition is not desirable. Hence, an optimized tool path algorithm with minimum start-stop points should be employed. Upon creating a suitable tool path algorithm, a proper volumetric flow rate of the ceramic slurry should be extruded and deposited. An improper combination of extrusion flow rate, nozzle diameter, and nozzle/stage speed leads to an inappropriate 3D-printed object. Another important parameter with a considerable effect on the quality of a ceramic 3D-printed object is the platform temperature affecting the pseudoplastic to dilatant transition upon ceramic filament extrusion and deposition [16].

Sintering: After ceramic 3D-printing, the produced green body still contains some solvent and organics. The green body is then dried to evaporate the remaining solvent and heat-treated

to $>1600^{\circ}\text{C}$ at $2^{\circ}\text{C}/\text{min}$ to decompose the organic additives and increase its density and strength [14,15].

4. Experiment and uncertainty analysis

4.1. Experimental test setup

Fig. 4 shows a schematic of the air-to-air HX test loop facility and a closed-view image of the HX test section including integrated pressure and temperature sensors. Air was employed as the working fluid for both hot and cold flow streams. An in-line electrical heater (Model: Sureheat F038823) was utilized to heat the hot-side air stream to the desired test temperature. Four ungrounded K-type thermocouples (Model: Omega M12KIN-1/8-U-6-D) with an accuracy of $\pm 2.2^{\circ}\text{C}$ were employed to measure air temperature at the inlet and outlet sections of the HX test section. Four pressure transducers (Model: Setra ASM1-020B-A) with an uncertainty of $\pm 0.1\%$ reading were used to measure pressure drop across the HX module. Additionally, the mass flow rate was measured using two Coriolis mass flow meters (Model: Emerson CMFS050HB) with an accuracy of 0.01 g/s . A data acquisition system (Model: Agilent 34972A LXI DAQ) was used to read and record temperature, pressure, and mass flow rate.

Table 2 lists the nominal test conditions, range, and uncertainty of main experimental parameters including air flow rate, temperature, and pressure. The inlet temperatures of the hot and cold streams vary from 250 to 700°C . It should be noted that thermal performances of the two ceramic HX types were not examined at the same mass flow rate range since the physical dimensions of the lung-inspired (i.e., $33.2 \times 33.3 \times 35.2\text{ mm}^3$) and plate-and-frame (i.e., $54 \times 51 \times 12\text{ mm}^3$) ceramic HXs were not similar. Instead, the hot and cold mass flow rates were chosen in such a way that a similar Reynolds (Re) number range was ensured for the two HX types. The hydraulic diameters of each HX type were considered as the characteristic lengths in the Re number calculations. The hydraulic diameter of the lung-inspired ceramic HX was calculated based upon the minimum cross-sectional flow area available. Additionally, each experimental test was allowed for at least 10 minutes to reach a steady-state condition at which there was no continuous rise and/or decline in air temperature, pressure, and mass flow rates.

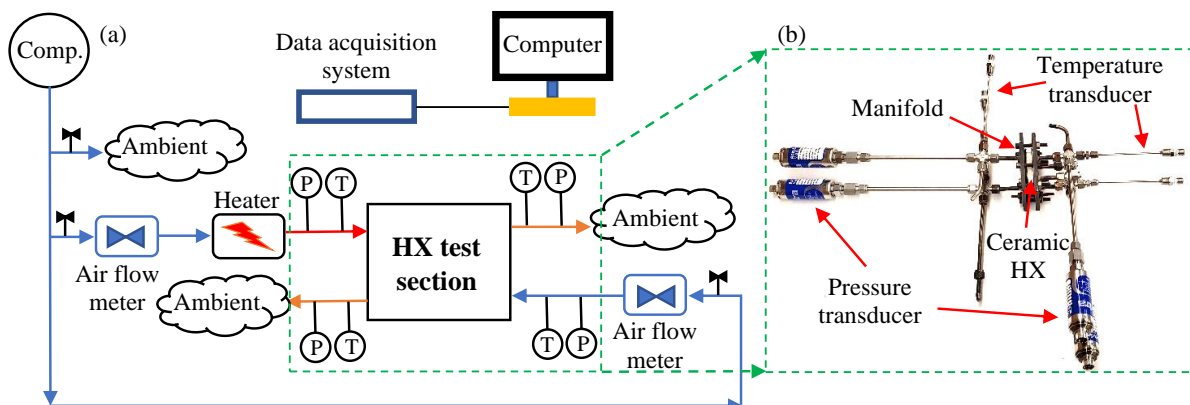


Fig. 4. (a) A schematic of the air-to-air HX test loop facility, and (b) an image of the HX test section.

Table 2. Nominal test conditions, range, and uncertainty of main parameters.

Parameters	Nominal test conditions		Operating range		Uncertainty
	Lung-inspired	Plate-and-frame	Lung-inspired	Plate-and-frame	
$T_{in,hot}$ (°C)	500	500	250 ~ 700	250 ~ 700	±2.2
$T_{in,cold}$ (°C)	25	25	22 ~ 28	22 ~ 28	±2.2
\dot{m}_{hot} (g/s)	0.843	1.74	1.12 ~ 1.92	0.703 ~ 0.89	±0.01
\dot{m}_{cold} (g/s)	0.384	0.67	0.38 ~ 0.77	0.29 ~ 0.478	±0.01
$Re_{hot,in}$	1326	1326	867 ~ 1476	1106 ~ 1400	±1%
$Re_{cold,in}$	1102	1102	615~1255	832 ~ 1372	±1%
$P_{hot,in}$ (bar)	2.41	2.85	2.01 ~ 3.02	1.92 ~ 2.53	±0.1%
$P_{cold,in}$ (bar)	1.14	1.33	1.18 ~ 1.5	1.08~1.23	±0.1%

4.2. Data reduction

The net thermal duty (\dot{Q}) exchanged between the hot and cold flow streams is defined as follows:

$$\dot{Q} = \dot{m}_{hot}c_{p,hot}(T_{hot,in} - T_{hot,out}) = \dot{m}_{cold}c_{p,cold}(T_{cold,out} - T_{cold,in}) \quad (1)$$

where \dot{m} and c_p are air mass flow rate and specific heat, respectively. The heat exchanger effectiveness (ε) is defined as the ratio of the net thermal duty to the maximum possible heat transfer rate (\dot{Q}_{max}) as follows:

$$\varepsilon = \dot{Q}_{ave}/\dot{Q}_{max} \quad (2)$$

where

$$\dot{Q}_{max} = (\dot{m}c_p)_{min}(T_{hot,in} - T_{cold,in}) \quad (3)$$

The maximum possible heat transfer rate between the hot and cold flow streams represents a hypothetical situation in which one fluid experiences the maximum possible temperature difference (i.e., $T_{hot,in} - T_{cold,in}$) in a counter-flow heat exchanger of infinite length. The maximum possible temperature difference is perceived by the fluid with the minimum heat capacity rate (i.e., $\dot{m}c_p$).

The logarithmic mean temperature difference (LMTD) of the HXs is also defined as follows:

$$\Delta T_{lm} = (\Delta T_1 - \Delta T_2)/\ln(\Delta T_1/\Delta T_2) \quad (4)$$

where

$$\Delta T_1 = (T_{hot,in} - T_{cold,out}) \quad (5)$$

$$\Delta T_2 = (T_{hot,out} - T_{cold,in}) \quad (6)$$

The UA value of the HXs can be obtained as follows:

$$UA = \dot{Q}/\Delta T_{lm} \quad (7)$$

where U is the overall heat transfer coefficient and A is the heat transfer area.

Additionally, the volume ($VBPD$) and mass-based power densities ($MBPD$) are also defined as the ratios of the net thermal duty to HX volume and mass, respectively, as follows:

$$VBPD = V/\dot{Q} \quad (8)$$

$$MBPD = M/\dot{Q} \quad (9)$$

where V and M are the volume and mass of the ceramic heat exchanger.

4.3. Uncertainty analysis

The uncertainty associated with a function F which is a function of X_1, X_2, \dots, X_n with uncertainties of $\delta X_1, \delta X_2, \dots, \delta X_n$ is calculated as follows [17]:

$$\delta F = \sqrt{\sum_i \left(\frac{\partial F}{\partial X_i}\right)^2 \delta X_i^2} \quad (10)$$

Therefore, the uncertainty associated with the HX thermal duty (\dot{Q}) can be calculated as:

$$\delta \dot{Q}/\dot{Q} = \sqrt{(\delta \dot{m}_{hot}/\dot{m}_{hot})^2 + (\delta \Delta T_{hot}/\Delta T_{hot})^2} \quad (11)$$

where ΔT is the temperature difference between the inlet and outlet sections. The uncertainty associated with the temperature difference can be calculated as:

$$\delta\Delta T = \sqrt{(\delta T_{in})^2 + (\delta T_{out})^2} \quad (12)$$

Using a similar approach, the uncertainties associated with effectiveness, $LMTD$, UA , $VBPD$, and $MBPD$ can be estimated as follows:

$$\delta\varepsilon/\varepsilon = \sqrt{(\delta\dot{Q}/\dot{Q})^2 + (\delta\dot{Q}_{max}/\dot{Q}_{max})^2} \quad (13)$$

$$\delta(LMTD) = \sqrt{\left(\frac{1 - \frac{1}{R} - \ln(R)}{(\ln(R))^2} \cdot \delta(\Delta T_2)\right)^2 + \left(\frac{R - 1 - \ln(R)}{(\ln(R))^2} \cdot \delta(\Delta T_1)\right)^2} \quad (14)$$

$$\frac{\delta(UA)}{UA} = \sqrt{\left(\frac{\delta\dot{Q}}{\dot{Q}}\right)^2 + \left(\frac{\delta LMTD}{LMTD}\right)^2} \quad (15)$$

$$\delta(VBPD)/VBPD = \sqrt{(\delta\dot{Q}/\dot{Q})^2 + (\delta V/V)^2} \quad (16)$$

$$\delta(MBPD)/MBPD = \sqrt{(\delta\dot{Q}/\dot{Q})^2 + (\delta M/M)^2} \quad (17)$$

where R is $\Delta T_2/\Delta T_1$. Also, $\delta(\Delta T_1)$, and $\delta(\Delta T_2)$ can be calculated as follows:

$$\delta(\Delta T_1) = \sqrt{(\delta T_{air,out})^2 + (\delta T_{water,in})^2} \quad (18)$$

$$\delta(\Delta T_2) = \sqrt{(\delta T_{air,in})^2 + (\delta T_{water,out})^2} \quad (19)$$

5. Numerical simulation

Experimental results were further analyzed by three-dimensional (3D) computational flow dynamic (CFD) simulations. Fluid flow was considered to be steady-state, laminar, and incompressible. The continuity, momentum, and energy equations can be written as:

$$\frac{\partial u_i}{\partial x_i} = 0 \quad (20)$$

$$u_j \frac{\partial u_i}{\partial x_j} = -\frac{1}{\rho} \frac{\partial P}{\partial x_i} + \vartheta \frac{\partial u_i}{\partial x_j \partial x_j} \quad (21)$$

where u , ρ , P , and ϑ are the velocity, density, pressure, and kinematic viscosity, respectively. The energy equation for air and solid materials can be expressed as follows:

$$u_j \frac{\partial T}{\partial x_j} = -\alpha \frac{\partial T}{\partial x_j \partial x_j} \quad (22)$$

where T and α are temperature and thermal diffusivity, respectively.

The above governing equations were solved in ANSYS Fluent software. First, a 3D model of the heat exchanger was created in SolidWorks software. Then, the HX geometry was imported to the SpaceClaim module of the ANSYS Workbench to designate fluid and solid bodies. The modified geometry was then discretized in the Meshing module of the ANSYS Workbench. Following a mesh independent study, a tetrahedral computational mesh type with an element size of 0.3 mm was chosen resulting in 11.8 and 16.5 million computational cells for the plate-and-frame and lung-inspired HXs, respectively. The CFD simulations were conducted under a steady-state condition and a laminar flow regime. The inlet and outlet boundary conditions were set as mass flow inlet and outflow conditions, respectively. Additionally, no-slip and isolated boundary conditions are considered for internal walls and external surfaces of the HXs, respectively. Table 3 lists thermo-physical properties of the working fluid and ceramic materials employed in the CFD modeling.

The CFD model was validated against the experimental results of the present study for the plate-and-frame alumina 3D-printed HX module as shown in Fig. 7. The thermal conductivity of alumina material 3D-printed through the robocasting technique was experimentally measured at different temperatures at Oak Ridge National Laboratory (ORNL) of the U.S. Department of Energy and employed in the CFD model (cf. Fig. 5). As evident in Fig. 7, the simulation results well predict the experimental data of the plate-and-frame alumina 3D-printed HX module at various hot inlet air temperatures with a maximum deviation of less than 5%. The validated model was then employed to estimate the thermal conductivity of the lung-inspired zirconia-coated silica 3D-printed HX module. This was necessary as the effective thermal conductivity of the lung-inspired silica 3D-printed HX module might have been affected by the zirconia-coated layer.

Table 3. Thermo-physical properties of different materials in CFD simulation at the nominal test condition.

Properties	Hot air	Cold air	Alumina	Silica
Density (kg/m ³)	0.991	1.153	3900	2600
Thermal conductivity (W/m-K)	0.0519	0.0365	Fig. 5	Fig. 5
Specific heat (J/kg-K)	1076	1019	780	730
Viscosity (kg/m-s)	3.35×10^{-5}	2.35×10^{-5}	-	-

6. Results and discussion

6.1. Effective thermal conductivity of the zirconia-coated silica 3D-printed HX

The effective thermal conductivity of the lung-inspired silica 3D-printed HX module is affected by the zirconia-coated layer. Therefore, the experimentally measured thermal performance data of the lung-inspired zirconia-coated silica HX module were compared against those of numerical simulations conducted at different thermal conductivities. The zirconia thermal conductivity is slightly higher than the silica thermal conductivity. Therefore, the thermal conductivity of the zirconia coated silica was considered to be a coefficient of the base silica thermal conductivity. The thermal conductivity

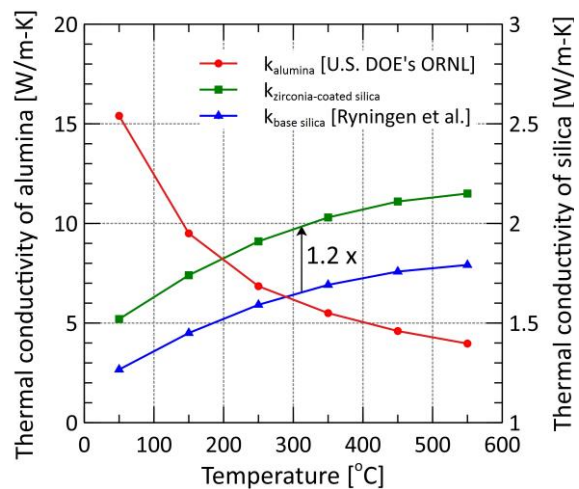


Fig. 5. Thermal conductivity of alumina, base silica, and zirconia-coated silica materials.

of the base silica is reported by Ryningen et al. [18] and shown in Fig. 5. A comparison between the experimental and numerical results confirmed that the thermal conductivity of the zirconia-coated silica is 1.2 times higher than that of the base silica. Under this condition, the CFD model well predicts the experimental data at different hot inlet temperatures with a maximum deviation of less than 5% as shown in Fig. 7. It should be also noted that the numerical model was first validated against the experimental data of the plate-and-frame alumina 3D-printed HX module as discussed in section 5 and shown in Fig. 7.

Fig. 6 shows temperature contours of the air (main images) and solid (inset images) domains for the lung-inspired zirconia-coated silica and plate-and-frame alumina HX module at the nominal test conditions listed in Table 2. The CFD model also includes fluid flow through the

headers and inlet/outlet tubes. As evident, the lung-inspired HX module can volumetrically distribute the incoming hot air stream within and through the cold air stream. Under the nominal test conditions, the thermal duty of the lung-inspired and plate-and-frame HX modules are 218.7 and 119.7 W, respectively. The hot-side air inlet temperature decreases from 500°C to 383.2 and 367.9°C for the lung-inspired and plate-and-frame ceramic HX modules, respectively. Additionally, the cold-side air inlet temperature increases from 25°C to 344.3°C and 330.4°C for the lung-inspired and plate-and-frame ceramic HX modules, respectively.

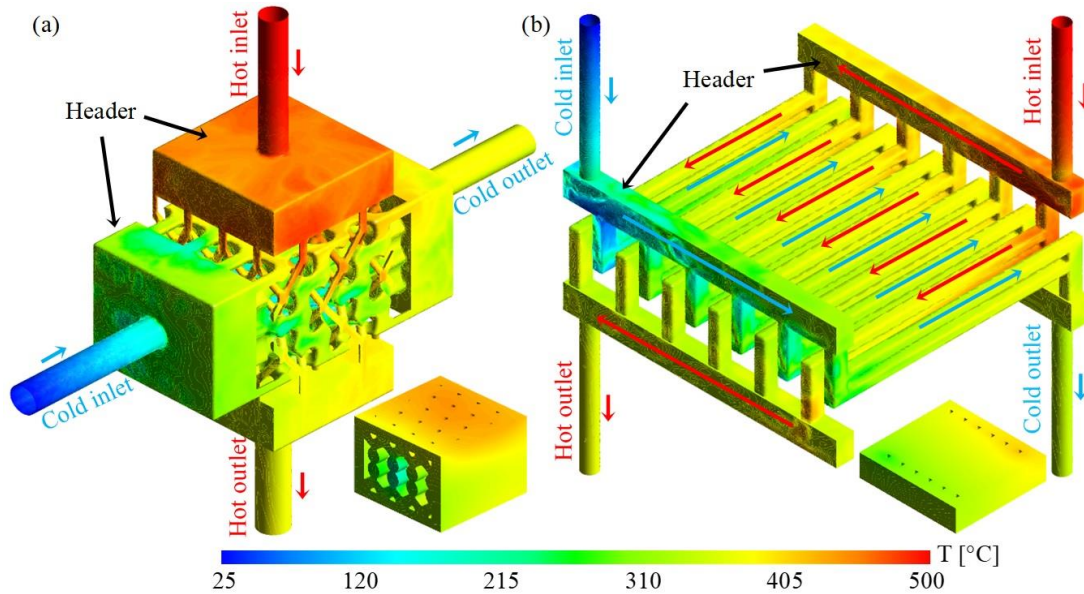


Fig. 6. Temperature contours of the air (main images) and solid (inset images) domains for (a) the lung-inspired, and (b) the plate-and-frame ceramic HX modules.

6.2. Thermo-hydraulic performance of the ceramic 3D-printed HXs

In this section, the effect of the hot air inlet temperature and hot/cold air mass flow rate on the thermo-hydraulic performance of the ceramic 3D-printed HXs are studied. Fig. 7a shows VBPD of the lung-inspired and plate-and-frame ceramic 3D-printed HXs as a function of the hot air Re number. The Re number of the cold side was kept constant at 1102. The air inlet temperatures of the hot and cold sides were also fixed at 500 and 25°C, respectively. As shown, the simulation results well predict the experimental data at different hot-side air Re numbers with a maximum deviation of less than 5%. The VBPD values of both ceramic HX types increase with the hot-side air mass flow rate. This is attributed to the convective heat transfer coefficient, which increases at higher air mass flow rates. As evident, the VBPD of the lung-inspired zirconia-coated silica 3D-printed HX is substantially higher than that of the plate-and-frame alumina 3D-printed HX module. For instance, at a hot-side air Re number of 1326, the VBPD of the lung-inspired HX is 6.7 MW/m³, while the VBPD of the plate-and-frame HX is 3.35 MW/m³. This is attributed to an improved volumetric flow distribution and thus an efficient heat transfer process offered by the lung-inspired HX design. More importantly, the higher thermal performance of the lung-inspired zirconia-coated silica HX is achieved at a lower normalized pressure drop penalty than that of the plate-and-frame alumina HX as shown in Fig. 7b. For instance, at a hot-side air Re number of 1326, the normalized pressure drop of the lung-inspired ceramic HX is 510 Pa/W, which is 22% lower than that of the plate-and-frame ceramic HX. It should be noted that a normalized pressure drop penalty, defined as the

pressure drop divided by the HX thermal duty, was employed since the overall physical dimensions of the lung-inspired (i.e., $33.2 \times 33.3 \times 35.2 \text{ mm}^3$) and plate-and-frame (i.e., $54 \times 51 \times 12 \text{ mm}^3$) HXs were not the same. Furthermore, the normalized pressure drop penalties of both ceramic 3D-printed HX types increase with the air mass flow rate due to augmented frictional pressure losses. Therefore, the bronchi arrangement of the lung-inspired ceramic HX design allows high thermal duties at reduced pressure drop penalties.

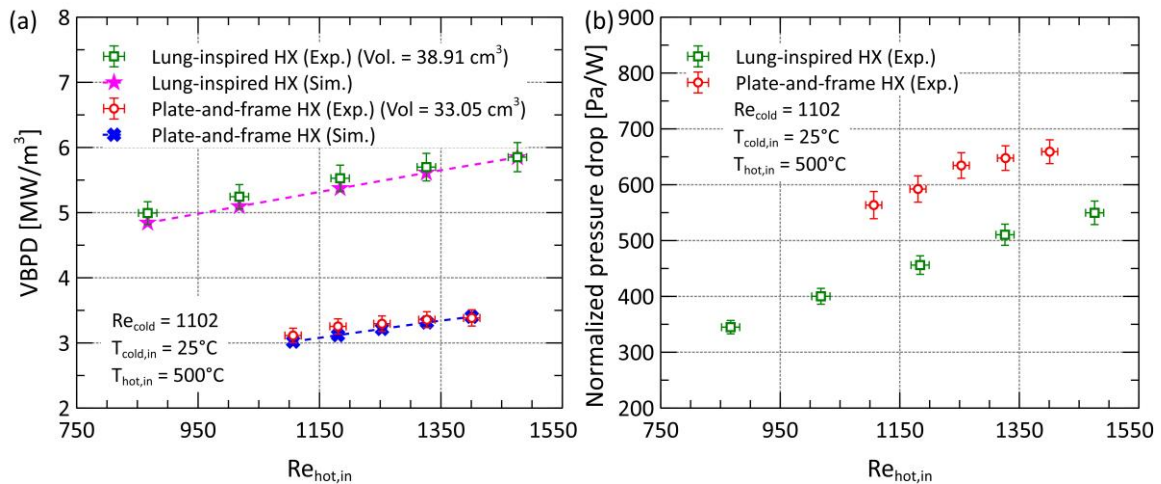


Fig. 7. Variations of (a) VBPD, and (b) hot-side normalized pressure drop penalty of the lung-inspired and plate-and-frame ceramic 3D-printed HXs versus the hot-side air Reynolds number.

Fig. 8 shows the experimentally measured UA value and effectiveness of the lung-inspired and plate-and-frame ceramic HXs as a function of the hot-side air Re number. As shown in Fig. 8a, the UA values of both ceramic HX types increase with the hot-side air mass flow rate (i.e., Re number) due to an augmented heat transfer coefficient. However, the slope of the curve is higher for the lung-inspired ceramic 3D-printed HX compared with the plate-and-frame ceramic 3D-printed HX module. In other words, the heat transfer coefficient of the lung-inspired HX module is more augmented by the air mass flow rate compared with that of the plate-and-frame HX module. This indicates that the volumetric flow distribution offered by the lung-inspired HX design and supported by the two intertwined bicontinuous flow networks becomes more efficient at higher mass flow rates. Additionally, Fig. 8b shows that the HX

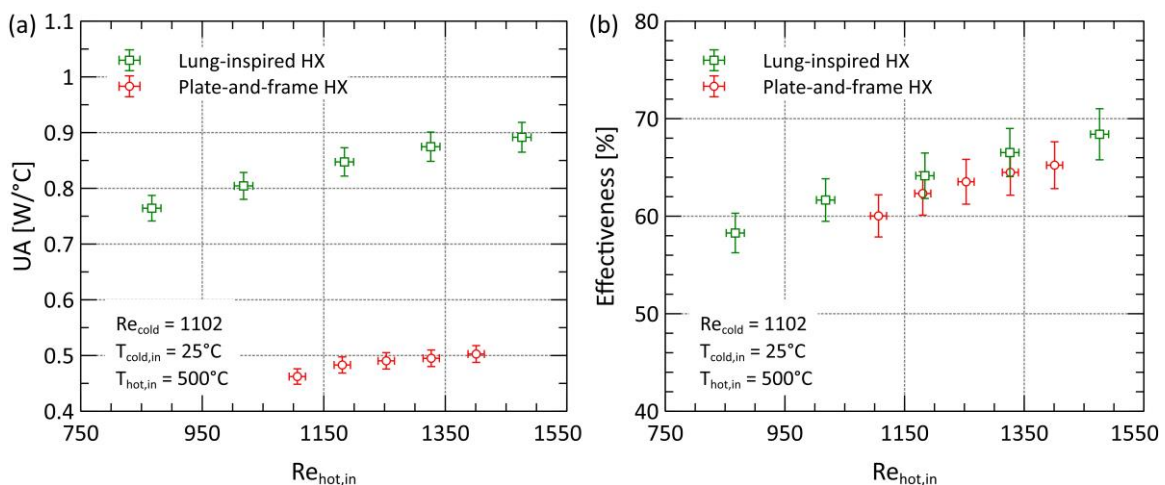


Fig. 8. Variations of (a) UA value, and (b) effectiveness of the lung-inspired and plate-and-frame ceramic 3D-printed HXs versus the hot-side air Reynolds number.

effectiveness of both lung-inspired and plate-and-frame ceramic 3D-printed HX modules increase with the hot-side air mass flow rate. The heat capacity rate (i.e., $\dot{m}c_p$) of the cold air stream is lower than that of the hot air stream. Therefore, the minimum heat capacity rate and thus the maximum possible heat transfer rate remains constant with the hot air mass flow rate. Under this condition, a rise in the actual HX thermal duty with the hot air mass flow rate results in a rise in the HX effectiveness as shown in Fig. 8b. In other words, a larger fraction of the maximum possible heat transfer rate is exchanged at higher hot air mass flow rates. Specifically, at a hot air Re number of 1476, the lung-inspired zirconia-coated silica 3D-printed HX module offers an exceptionally high HX effectiveness of 69% which is comparable with metal HXs.

Fig. 9a shows VBPD of the lung-inspired and plate-and-frame ceramic 3D-printed HXs as a function of the hot air inlet temperature. The Re numbers of the hot and cold sides were kept constant at 1326 and 1102, respectively. The cold air inlet temperature was also fixed at 25°C. The experimental results show that the VBPDs of both ceramic HX types increase with the hot air inlet temperature. For instance, increasing the hot air inlet temperature from 300 to 700°C improves the VBPDs of the lung-inspired and plate-and-frame ceramic HXs from 3.25 to 8.2 MW/m³ (i.e., a 151% improvement) and 1.98 to 4.75 MW/m³ (i.e., a 140% improvement), respectively. This is attributed to the logarithmic mean temperature difference (i.e., LMTD), which increases at higher hot air inlet temperatures, thereby increasing the HX thermal duty and VBPD. The simulation results also closely predict the experimental data with a maximum deviation of less than 5%. Additionally, the results demonstrate that the thermal performance of the lung-inspired HX is significantly higher than that of the plate-and-frame HX. For example, the VMPD of the lung-inspired ceramic HX is 71% higher than that of the plate-and-frame ceramic HX at a hot air inlet temperature of 700°C. This again emphasizes that the lung-inspired HX offers an exceptional design with an augmented heat transfer coefficient and thermal duty for high-temperature applications. Additionally, Fig. 9b shows the effectiveness of both ceramic 3D-printed HX types remains almost constant versus the hot air inlet temperature. This indicates that both the actual HX thermal duty and the maximum possible heat transfer rate increase at the same rate with an increase in the hot air inlet temperature.

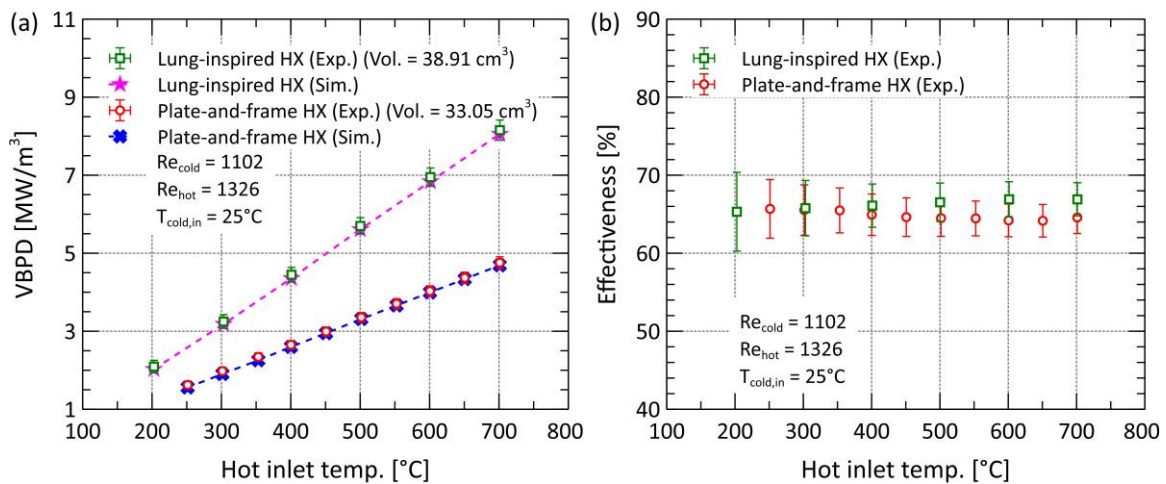


Fig. 9. Variations of (a) VBPD, and (b) HX effectiveness of the lung-inspired and plate-and-frame ceramic 3D-printed HXs versus the hot-side air inlet temperature.

Fig. 10 shows VBPD and MBPD of the lung-inspired and plate-and-frame ceramic 3D-printed HX modules as a function of the cold air Re number. As evident, the VBPD and MBPD of both ceramic HX types increase with the cold air Re number. This is attributed to the heat transfer coefficient, which increases at higher air mass flow rates, thereby increasing the HX thermal duty and subsequently VBPD and MBPD metrics. Additionally, the lung-inspired zirconia-coated silica HX significantly outperforms the plate-and-frame alumina HX in terms of both VBPD and MBPD metrics for all cold air mass flow rates examined. For instance, at a cold air Re number of 1102, the VBPD and MBPD of the lung-inspired HX topology are 170% and 261% higher than those of the plate-and-frame HX design, respectively. This again confirms the lung-inspired ceramic HX module offers a superior topology for enhanced high-temperature heat transfer applications.

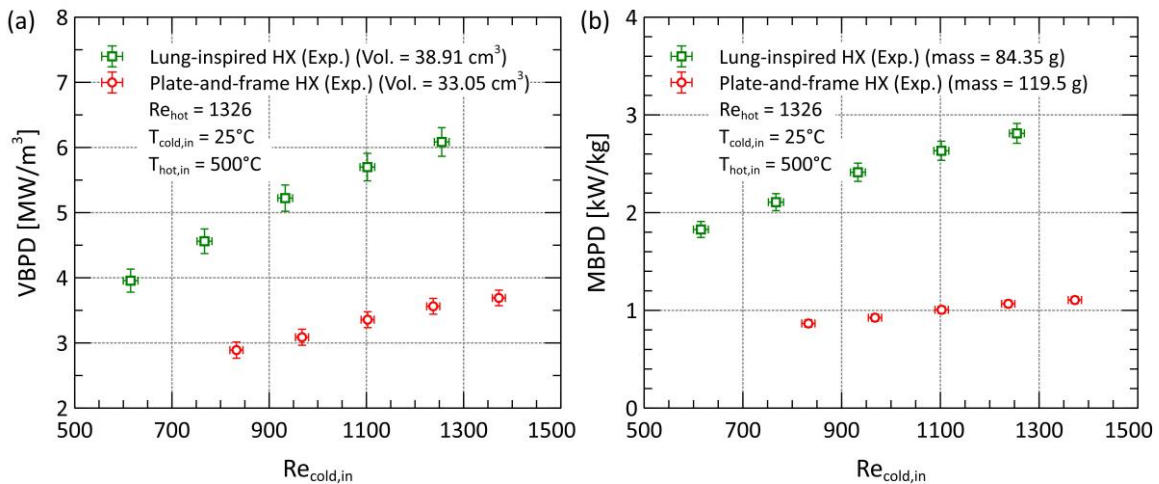


Fig. 10. Variations of (a) VBPD, and (b) MBPD of the lung-inspired and plate-and-frame ceramic 3D-printed HXs versus the cold-side air Reynolds number.

Fig. 11 shows a comparison between VBPD and hot-side air normalized pressure drop values of the lung-inspired zirconia-coated silica and plate-and-frame alumina 3D-printed HXs. The VBPD of the lung-inspired ceramic HX increases from 5 to 5.9 MW/m³ when the hot-side normalized pressure drop penalty varies from 350 to 550 Pa/W. In contrast, the VBPD of the plate-and-frame ceramic HX increases from 3.1 to 3.4 MW/m³ when the hot-side normalized pressure drop penalty varies from 560 to 660 Pa/W. Therefore, the lung-inspired ceramic HX demonstrates a higher VBPD value at a lower normalized pressure drop penalty compared with the plate-and-frame ceramic HX module.

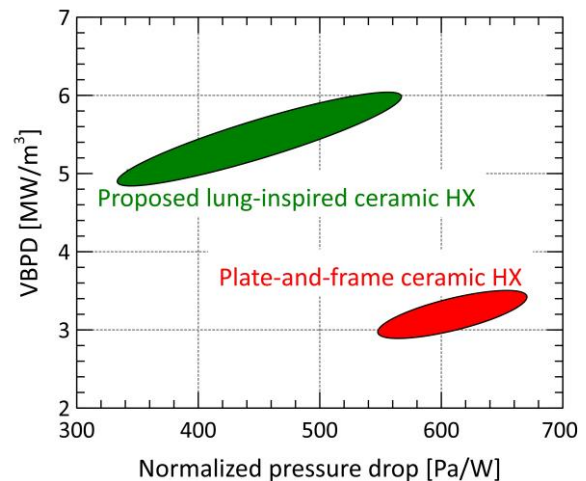


Fig. 11. A comparison between the VBPD and hot-side air normalized pressure drop penalty of the lung-inspired zirconia-coated silica and plate-and-frame alumina 3D-printed HXs.

7. Conclusion

In this study, a novel leak-free lung-inspired ceramic 3D-printed HX topology was introduced for high-temperature energy applications. The gas leakage (i.e., permeability) issue associated with thin separating walls of a ceramic stereolithography-based 3D-printed HX

design was resolved by a zirconia-coated layer. The high-temperature thermo-hydraulic characteristics of the lung-inspired ceramic 3D-printed HX design were compared against those of a plate-and-frame ceramic robocasted 3D-printed HX design. Although restricting the design freedom, the ceramic robocasted 3D-printing results in leak-free HX modules without requiring any post-treatment steps due to a small fraction of organic additives employed.

It was identified that the zirconia-coated layer improves the effective thermal conductivity of the lung-inspired silica 3D-printed HX by 20%. The results showed that the lung-inspired ceramic 3D-printed HX topology offers a higher volume-based power density at a reduced normalized pressure drop penalty compared with the plate-and-frame ceramic HX design. This is because the lung-inspired HX topology leverages two intertwined bicontinuous flow networks allowing a volumetric flow distribution of the hot air stream within and through the cold air stream with an enhanced heat transfer process. The lung-inspired ceramic HX offers a volume-based power density of 8.2 MW/m³ and a normalized pressure drop penalty of 510 Pa/W at an inlet hot-side air temperature of 700°C, which are a 71% improvement and a 22% reduction compared with those of the plate-and-frame ceramic HX, respectively. The results presented here suggest that the ceramic 3D-printed HX modules employing complex heat transfer topologies offer new pathways for next-generation, high-temperature, energy-efficient energy applications.

Acknowledgments

This study was sponsored by the Advanced Research Projects Agency-Energy (ARPA-E), U.S. Department of Energy, under Award Number DE-AR0001126. The authors would like to acknowledge Prof. Michael Ohadi, Program Manager, Prof. Zak Fang, Program Manager, Dr. Pankaj Trivedi, Tech-SETA, and Dr. Vivien Lecoustre, Tech-SETA of ARPA-E's HITEMMP (High Intensity Thermal Exchange through Materials and Manufacturing Processes) program.

References

- [1] Caccia M, Tabandeh-Khorshid M, Itskos G, Strayer AR, Caldwell AS, Pidaparti S, et al. Ceramic–metal composites for heat exchangers in concentrated solar power plants. *Nature* 2018;562:406–9. <https://doi.org/10.1038/s41586-018-0593-1>.
- [2] Mylavarapu S, Sun X, Figley J, Needler N, Christensen R. Investigation of high-temperature printed circuit heat exchangers for very high temperature reactors. *J Eng Gas Turbines Power* 2009;131:1–7. <https://doi.org/10.1115/1.3098425>.
- [3] Kwon JG, Kim TH, Park HS, Cha JE, Kim MH. Optimization of airfoil-type PCHE for the recuperator of small scale brayton cycle by cost-based objective function. *Nucl Eng Des* 2016;298:192–200. <https://doi.org/10.1016/j.nucengdes.2015.12.012>.
- [4] Schmidt J, Scheiffele M, Crippa M, Peterson PF, Urquiza E, Sridharan K, et al. Design, fabrication, and testing of ceramic plate-type heat exchangers with integrated flow channel design. *Int J Appl Ceram Technol* 2011;8:1073–86. <https://doi.org/10.1111/j.1744-7402.2010.02573.x>.
- [5] Banerjee A, Chandran RB, Davidson JH. Experimental investigation of a reticulated porous alumina heat exchanger for high temperature gas heat recovery. *Appl Therm Eng* 2015;75:889–95. <https://doi.org/10.1016/j.applthermaleng.2014.10.033>.
- [6] Kee RJ, Almand BB, Blasi JM, Rosen BL, Hartmann M, Sullivan NP, et al. The design, fabrication, and evaluation of a ceramic counter-flow microchannel heat exchanger. *Appl Therm Eng* 2011;31:2004–12. <https://doi.org/10.1016/j.applthermaleng.2011.03.009>.

- [7] Fend T, Völker W, Miebach R, Smirnova O, Gonsior D, Schöllgen D, et al. Experimental investigation of compact silicon carbide heat exchangers for high temperatures. *Int J Heat Mass Transf* 2011;54:4175–81. <https://doi.org/10.1016/j.ijheatmasstransfer.2011.05.028>.
- [8] Haunstetter J, Dreißigacker V, Zunft S. Ceramic high temperature plate fin heat exchanger: Experimental investigation under high temperatures and pressures. *Appl Therm Eng* 2019;151:364–72. <https://doi.org/10.1016/j.applthermaleng.2019.02.015>.
- [9] Schwarzer E, Götz M, Markova D, Stafford D, Scheithauer U, Moritz T. Lithography-based ceramic manufacturing (LCM) – Viscosity and cleaning as two quality influencing steps in the process chain of printing green parts. *J Eur Ceram Soc* 2017;37:5329–38. <https://doi.org/10.1016/j.jeurceramsoc.2017.05.046>.
- [10] Scheithauer U, Schwarzer E, Moritz T, Michaelis A. Additive Manufacturing of Ceramic Heat Exchanger: Opportunities and Limits of the Lithography-Based Ceramic Manufacturing (LCM). *J Mater Eng Perform* 2018;27:14–20. <https://doi.org/10.1007/s11665-017-2843-z>.
- [11] Shulman H, Nicole R. Additive Manufacturing for Cost Efficient Production of Compact Ceramic Heat Exchangers and Recuperators. *NETL Cross-Cutting Res Conf* 2015.
- [12] Bower C, Ortega A, Skandakumaran P, Vaidyanathan R, Phillips T. Heat transfer in water-cooled silicon carbide milli-channel heat sinks for high power electronic applications. *J Heat Transfer* 2005;127:59–65. <https://doi.org/10.1115/1.1852494>.
- [13] Lewis JA, Smay JE, Stuecker J, Cesarano J. Direct ink writing of three-dimensional ceramic structures. *J Am Ceram Soc* 2006;89:3599–609. <https://doi.org/10.1111/j.1551-2916.2006.01382.x>.
- [14] Cesarano J, Calvert PD. Freeforming objects with low-binder slurry. *US Pat* 2000.
- [15] Baer TA, Cesarano III J, Calvert P, Cesarano J, Baer TA, Calvert P. Recent developments in freeform fabrication of dense ceramics from slurry deposition. *Solid Free Fabr Proceedings*, Sept 1997 1997:25–32.
- [16] Cesarano J. A review of robocasting technology. *Mater Res Soc Symp - Proc* 1999;542:133–9. <https://doi.org/10.1557/proc-542-133>.
- [17] Taylor BN, Kuyatt CE. NIST Technical Note 1297 Guidelines for Evaluating and Expressing the Uncertainty of NIST Measurement Results. *NIST Tech Note* 1297 1994.
- [18] Rynningen B, Bellmann MP, Kvande R, Lohne O. The effect of crucible coating and the temperature field on minority carrier. *Eupvsec* 2012 2012:926–32. <https://doi.org/10.4229/27thEUPVSEC2012-2AV.4.2>.